

## Engineering of the Curie temperature of epitaxial $\text{Sr}_{1-x}\text{Ba}_x\text{TiO}_3$ films via strain

Y. Dai, J. Schubert, E. Hollmann, G. Mussler, and R. Wördenweber

Citation: *Journal of Applied Physics* **120**, 114101 (2016); doi: 10.1063/1.4962853

View online: <http://dx.doi.org/10.1063/1.4962853>

View Table of Contents: <http://scitation.aip.org/content/aip/journal/jap/120/11?ver=pdfcov>

Published by the [AIP Publishing](#)

---

### Articles you may be interested in

[Effect of crystal orientation on the phase diagrams, dielectric and piezoelectric properties of epitaxial  \$\text{BaTiO}\_3\$  thin films](#)

*AIP Advances* **6**, 015309 (2016); 10.1063/1.4940205

[Compositional engineering of  \$\text{BaTiO}\_3/\(\text{Ba},\text{Sr}\)\text{TiO}\_3\$  ferroelectric superlattices](#)

*J. Appl. Phys.* **114**, 104102 (2013); 10.1063/1.4820576

[Unusual  \$90^\circ\$  domain structure in  \$\(2/3\)\text{Bi}\(\text{Zn}\_{1/2}\text{Ti}\_{1/2}\)\text{O}\_3-\(1/3\)\text{BiFeO}\_3\$  epitaxial films with giant 22% tetragonal distortion](#)

*Appl. Phys. Lett.* **103**, 042904 (2013); 10.1063/1.4816420


[Strain relaxation of epitaxial  \$\(\text{Ba}\_{0.6}\text{Sr}\_{0.4}\)\(\text{Zr}\_{0.3}\text{Ti}\_{0.7}\)\text{O}\_3\$  thin films grown on  \$\text{SrTiO}\_3\$  substrates by pulsed laser deposition](#)

*J. Appl. Phys.* **107**, 106101 (2010); 10.1063/1.3380528

[Lattice strain in epitaxial  \$\text{BaTiO}\_3\$  thin films](#)

*Appl. Phys. Lett.* **88**, 152908 (2006); 10.1063/1.2194231

---

The advertisement features a large, industrial-grade laser system with a prominent yellow light output. To the left, a control rack with multiple modules and a monitor is visible. The background is dark, making the laser and its components stand out. The text 'High Energy Nanosecond Lasers' is written in a large, white, serif font at the top left. On the right, a list of features is provided: 'Energies to 1kJ', 'Variable Pulsewidths', and 'Intuitive GUI for system control'. The Continuum logo is displayed in a large, red, serif font at the bottom right, with the website address 'www.continuumlasers.com' below it.

*High Energy Nanosecond Lasers*

- Energies to 1kJ
- Variable Pulsewidths
- Intuitive GUI for system control

**Continuum**  
[www.continuumlasers.com](http://www.continuumlasers.com)

# Engineering of the Curie temperature of epitaxial $\text{Sr}_{1-x}\text{Ba}_x\text{TiO}_3$ films via strain

Y. Dai,<sup>a)</sup> J. Schubert, E. Hollmann, G. Mussler, and R. Wördenweber  
 Peter Grünberg Institute (PGI), Forschungszentrum Jülich, D-52425 Jülich, Germany

(Received 9 May 2016; accepted 2 September 2016; published online 20 September 2016)

The impact of strain on the structural and electrical properties of epitaxial  $\text{Sr}_{1-x}\text{Ba}_x\text{TiO}_3$  films grown on single crystalline  $\text{DyScO}_3$  (110),  $\text{TbScO}_3$  (110), and  $\text{GdScO}_3$  (110) substrates is presented. X-ray diffraction measurements demonstrate that all films are grown epitaxially. The tensile in-plane strain is only partially compensated by a contraction of the out-of-plane lattice parameter. As a result, the volume of the unit cell of the  $\text{Sr}_{1-x}\text{Ba}_x\text{TiO}_3$  film increases due to the tensile strain, and the resulting Poisson ratio of the film is  $\nu \approx 0.33$ , which is larger than but still close to the literature values of  $\nu \approx 0.23$  for unstrained defect-free  $\text{SrTiO}_3$ . The Curie temperature derived from the temperature dependence of the in-plane dielectric response leads to a strain-temperature phase diagram for the epitaxial  $\text{Sr}_{1-x}\text{Ba}_x\text{TiO}_3$  films. The experimental data show a deviation from the linear dependence predicted by the Landau thermodynamic theory for large strain ( $>1.2\%$ ). However, using the equilibrium thermodynamic analysis, we can demonstrate that this deviation arises from the relaxation of the strain due to defect formation in the film. The result reveals that in addition to the nominal misfit strain, the defect formation strongly affects the effective strain and, thus, the dielectric response of epitaxially grown ferroelectric films. *Published by AIP Publishing.* [<http://dx.doi.org/10.1063/1.4962853>]

## INTRODUCTION

Ferroelectric materials ranging from hydrogen-bonded crystals to ternary oxides (e.g., titanate or niobate) are prized for their extraordinary dielectric, pyroelectric, elastoelectric, and opto-electric properties and, therefore, are of interest for technical applications.<sup>1</sup> In particular, thin film ternary oxide ferroelectrics are ideal for use in data storage, sensors, actuators, and radio-frequency devices.<sup>2</sup> In particular, oxide ferroelectrics show profound features, e.g., giant permittivity, large piezoelectricity, or tunability, in the range of the phase transition temperature from the ferroelectric to the dielectric state. However, this temperature regime is typically far from room temperature. For instance, the Curie temperatures ( $T_C$ ) are 37 K for  $\text{SrTiO}_3$ ,<sup>3</sup> 403 K for  $\text{BaTiO}_3$ ,<sup>4</sup> 503 to 760 K (depending on the composition) for  $\text{PbZr}_{1-x}\text{Ti}_x\text{O}_3$ ,<sup>5</sup> 763 K for  $\text{PbTiO}_3$ ,<sup>6</sup> and 628 K for  $\text{NaNbO}_3$ .<sup>7</sup> In order to obtain desirable operating temperatures for these oxides, it is therefore necessary to modify  $T_C$  for these materials. This engineering of  $T_C$  could be achieved via strain, doping, or a combination of both. It has been shown for a number of perovskites,<sup>8–14</sup> tungsten bronzes,<sup>15,16</sup> and bismuth layer-structured ferroelectrics<sup>17,18</sup> that the clamp effect induces strain in epitaxial films resulting in a shift of  $T_C$ .

In this paper, we report a systematic study of the impact of strain on the Curie temperature of  $\text{Sr}_{1-x}\text{Ba}_x\text{TiO}_3$  (SBTO) films. Using the combination of SBTO with  $x \leq 0.37$  and various rare earth scandate substrates, we varied the in-plane lattice strain of the films from 0% to 1.7%. The electronic analysis of the films shows a systematic shift of the Curie temperature, which is correlated with the in-plane strain.

Using simple theoretical models, which consider the strain-generated formation of defects in the film and their impact on the strain relaxation, we can explain the correlation between the Curie temperature and the strain modified structure of these films.

## EXPERIMENTAL TECHNIQUES AND SAMPLE PREPARATION

Strained SBTO films with  $x = 0, 0.125$ , and  $0.37$  were grown on  $\text{DyScO}_3$  (110),  $\text{TbScO}_3$  (110), and  $\text{GdScO}_3$  (110) single crystalline substrates via pulsed-laser deposition (PLD) using sintered ceramic targets with stoichiometric  $\text{SrTiO}_3$ ,  $\text{Sr}_{0.875}\text{Ba}_{0.125}\text{TiO}_3$ , and  $\text{Sr}_{0.63}\text{Ba}_{0.37}\text{TiO}_3$ , respectively. The laser power was  $5 \text{ J/cm}^2$  with a repetition rate of 1 Hz, the process gas was oxygen at a pressure of 1 Pa, and the growth temperature was  $700^\circ\text{C}$ .<sup>19</sup> In order to obtain relatively homogeneously strained epitaxial films with still reasonably large capacitive contributions, a layer thickness of 40 nm was chosen for all samples. For the analysis of the in-plane dielectric properties of the film, interdigitated electrodes (IDEs) were prepared on top of the SBTO layer using e-beam lithography and a lift-off technique. The IDEs were made from a 5 nm thick Cr layer for adhesion and a 15 nm thick Pt layer. The interdigitated structure consisted of 64 “fingers.” In order to simplify the data analysis, a relatively large gap of  $5 \mu\text{m}$  was chosen in combination with a large effective capacitor length of  $63 \times 700 \mu\text{m} = 44.1 \text{ mm}$ .<sup>10</sup> The former allows the use of the partial capacitive model,<sup>20</sup> and the latter leads to sufficient resolution of the capacitive measurement. The surface of the  $\text{DyScO}_3$  (110),  $\text{TbScO}_3$  (110), and  $\text{GdScO}_3$  (110) substrates exhibited a nearly square lattice with only a small difference between the  $[1\bar{1}0]$  and  $[001]$

<sup>a)</sup>y.dai@fz-juelich.de

TABLE I. Lattice parameters (accuracy:  $\pm 0.001 \text{ \AA}$ ) and resulting nominal strain of our strained SBTO films. The lattice parameters  $a_{ref}$  represent the literature value of the unstrained material. Furthermore, corrected values of the strain using a Poisson ratio  $\nu = 0.23$  (literature value for unstrained SBTO) are given in parentheses. The correction will be discussed later in this paper.

Abbreviation	Film	Substrate	Reference $a_{ref}$	Lattice parameters of the film ( $\text{\AA}$ )			Resulting strain (%)		
				Experiment value			$\epsilon_a$	$\epsilon_b$	$\epsilon_c$
				a	b	c			
A	$\text{Sr}_{0.63}\text{Ba}_{0.37}\text{TiO}_3$	DyScO <sub>3</sub>	3.939	3.951	3.945	3.939	0.305 (0.219)	0.152 (0.067)	0.000 (−0.085)
B	$\text{Sr}_{0.875}\text{Ba}_{0.125}\text{TiO}_3$	DyScO <sub>3</sub>	3.916	3.949	3.940	3.901	0.843 (0.810)	0.613 (0.580)	−0.383 (−0.415)
C	$\text{SrTiO}_3$	DyScO <sub>3</sub>	3.904	3.951	3.946	3.882	1.204 (1.130)	1.076 (1.002)	−0.564 (−0.637)
D	$\text{SrTiO}_3$	TbScO <sub>3</sub>	3.904	3.964	3.962	3.877	1.537 (1.403)	1.486 (1.352)	−0.692 (−0.823)
E	$\text{SrTiO}_3$	GdScO <sub>3</sub>	3.904	3.971	3.966	3.875	1.716 (1.561)	1.588 (1.433)	−0.743 (−0.894)

directions, which we will call the “short” and “long” axes in the following. As a consequence, the epitaxial films experienced a different in-plane strain for the two different directions. For the (110) DyScO<sub>3</sub> substrates, the [001] direction represents the “long” axis, whereas the  $[1\bar{1}0]$  direction is the “long” axis for the (110) TbScO<sub>3</sub> and (110) GdScO<sub>3</sub> substrates. The nominally cubic SBTO adapts the in-plane rectangular lattice structure of the different substrates. The in-plane primitive translation vectors [100] and [010] of SBTO are elongated and oriented along the  $[110]$  and  $[001]$  directions of the substrate, respectively, whereas the [001] lattice parameter of SBTO is oriented normal to the substrate surface.<sup>10</sup>

All samples are equipped with two IDE structures, one with the electric field  $\vec{E}$  aligned along the short axis and the other one with  $\vec{E}$  aligned along the long axis. The capacitance and losses are measured by an LCR meter (ST2826 Sourcetronic) with an ac field of  $5 \times 10^{-8} \text{ V/m}$  at 10 kHz in a temperature regime from 10 K to 450 K. The stoichiometry, roughness, and structure are analyzed prior to cryoelectronic characterization. The stoichiometry of the films is checked by Rutherford back-scattering spectrometry. The surface roughness of the films is determined by atomic force microscopy. All samples are quite smooth, and the average roughness of the samples is better than  $R_a \cong 0.5 \text{ nm}$ . X-ray reciprocal space mapping (RSM) is used to analyze the crystalline properties and epitaxy of the films.

## EXPERIMENTAL RESULTS AND DISCUSSION

For the sake of clarity, we arranged the samples according to the strain and labeled them A (smallest strain) to E (largest strain): thus, sample A is  $\text{Sr}_{0.63}\text{Ba}_{0.37}\text{TiO}_3/\text{DyScO}_3$ , sample B is  $\text{Sr}_{0.875}\text{Ba}_{0.125}\text{TiO}_3/\text{DyScO}_3$ , sample C is  $\text{SrTiO}_3/\text{DyScO}_3$ , sample D is  $\text{SrTiO}_3/\text{TbScO}_3$ , and sample E is  $\text{SrTiO}_3/\text{GdScO}_3$  (see also Table I).

Fig. 1 shows a selection of RSM data obtained from XRD analysis of the two different in-plane orientations of the substrates for all samples. The upper and lower figures reveal the lattice correlation in the [001] and  $[1\bar{1}0]$  substrate directions, respectively. Fig. 1 demonstrates the high quality of the epitaxy for all films. The  $q_{\parallel}$ -values are identical for the film and the substrate, i.e., within the experimental accuracy, all in-plane lattice parameters of the films are matched to those of the respective substrate. As a consequence, the

difference between the lattice parameters of the strained and unstrained (crosses in Fig. 1) SBTO increases from sample A to E, i.e.,  $q_{\parallel}$  shifts to smaller values compared to the  $q_{\parallel}$  value of the unstrained reference, and  $q_{\perp}$  shifts to larger values compared to its unstrained counterpart. Thus, with increasing lattice mismatch between the film and substrate, the film experiences more and more strain. The tensile in-plane strain is partially compensated by a compressive out-of-plane strain. Using the RSM data, we can evaluate the lattice parameters and, thus, evaluate the nominal misfit strain of the films. Table I provides a summary of the lattice parameters and the resulting nominal misfit strain obtained from averaging the RSM data measured in the four different lattice directions (332),  $(3\bar{3}2)$ , (420), and (240).

In order to learn more about the structural changes induced by the strain, we calculate the in-plane areal lattice misfit and the volumetric change of the SBTO for all films. In a first approach, all misfit values are obtained via a comparison of the measured lattice parameters and the corresponding literature values for the unstrained material (see Table I). As such, these values represent nominal values for the  $c$ -axis lattice misfit, in-plane areal misfit, and volume mismatch. Later, we will show that these values have to be corrected due to structural relaxation effects that are caused by defects in the material. For small concentrations  $x$ , unstrained SBTO has a cubic lattice. Its lattice parameter shows a linear dependence on the change of the barium content at room temperature, which can be approximated by  $a_{ref} = 3.904 + 0.094x \text{ (\AA)}$  for  $0 \leq x < 0.6$ .<sup>21,22</sup> Using  $a_{ref}$ , we can evaluate the nominal lattice mismatch for each lattice parameter, e.g.,  $\epsilon_c = (c - a_{ref})/a_{ref}$ , the resulting in-plane area mismatch  $(ab - a_{ref}^2)/a_{ref}^2$ , and the volume mismatch  $(abc - a_{ref}^3)/a_{ref}^3$ . The nominal lattice mismatch is given in Table I. Additionally, the  $c$ -axis mismatch and the volume change are plotted as a function of the areal misfit in Fig. 2. The figure shows a linear decrease of the  $c$ -axis (out-of-plane) lattice parameter of the SBTO film with increasing areal mismatch, which indicates that the tensile in-plane strain is compensated by a shrinkage of the  $c$ -axis. However, this is only a partial compensation since the volume of the unit cell still increases with increasing areal mismatch as shown in Fig. 2. A very interesting point here is the linear dependence between the volumetric change and the in-plane strain. This not only reveals that the Poisson ratio  $\nu$  is

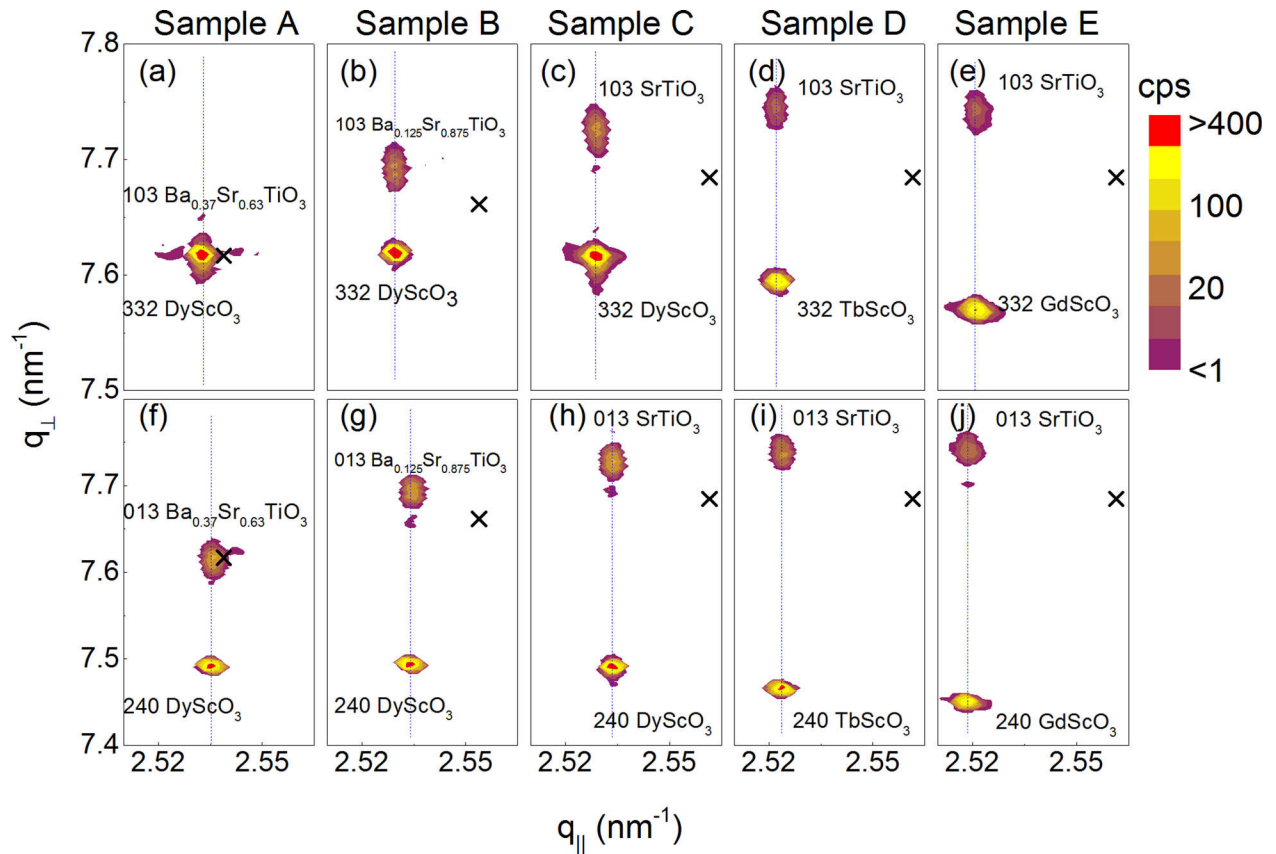


FIG. 1. RSM of the X-ray diffraction in the vicinity of the (332) (a)–(e) and the (240) (f)–(j) Bragg reflections of the substrates for samples A–E. The crosses mark the corresponding position of the reflection of unstrained SBTO for the respective stoichiometry.

identical for all SBTO films, but we can also derive the value of the Poisson ratio for the strained films. It turns out to be  $\nu \approx 0.33$ , which is larger than but still close to the literature value  $\nu \approx 0.23$  reported for unstrained crystalline  $\text{SrTiO}_3$ .<sup>23</sup> The increase of the Poisson ratio might be caused by defects in the films, which will be addressed later.

In the following, we will discuss the impact of the strain on the dielectric properties. We will restrict this discussion to the change of the Curie-Weiss temperature  $T_C$  caused by the strain. Generally, changes of the cell volume or lattice

parameters affect the ferroelectric phase transition. In SBTO, A-site cation substitution or alternatively mechanical pressure provides such an effect. This was simulated using, for instance, Ising-like model calculations<sup>24</sup> or a classical shell-model potential.<sup>25</sup> With increasing cell volume obtained by Ba-substitution or in-plane tensile strain, the potential well related to ferroelectric distortion becomes wider and deeper, and, as a consequence, the Curie-Weiss temperature is expected to rise. Therefore, the dielectric properties can strongly differ from those of the unstrained material. Understanding these effects is of importance for engineering the dielectric properties via strain.

The in-plane dielectric properties are measured along the two orientations for all samples to determine the Curie-Weiss temperature  $T_C$ . Fig. 3 shows typical data obtained for the permittivity and  $\tan \delta$  as a function of temperature. The peak in the permittivity and  $\tan \delta$  indicates the transition from the dielectric to the ferroelectric state.<sup>10</sup> The Curie-Weiss fit provides the exact  $T_C$  value for all samples (see dashed lines and their linear extrapolation in Fig. 3).

In order to analyze the impact of the strain on the Curie-Weiss temperature, we consider the change of  $T_C$  due to the strain. According to the literature,  $T_C$  of unstrained SBTO can be approximated by a polynomial fit

$$T_C = a_0 + a_1x - a_2x^2 \quad (1)$$

with coefficients  $a_0 = 30$  K,  $a_1 = 484$  K, and  $a_2 = -136$  K (Refs. 25–27); or  $a_0 = 36$  K,  $a_1 = 356$  K, and  $a_2 = 0$  K.<sup>28–30</sup>

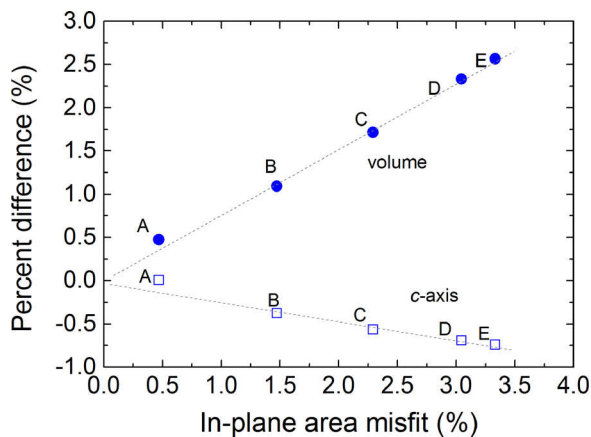


FIG. 2. Volume of the unit cell (solid circles) and  $c$ -axis (open squares) differences as a function of the in-plane areal mismatch for samples A–E. The data are evaluated from the X-ray diffraction data shown in Fig. 1; the dashed lines indicate the linear dependence for both parameters.



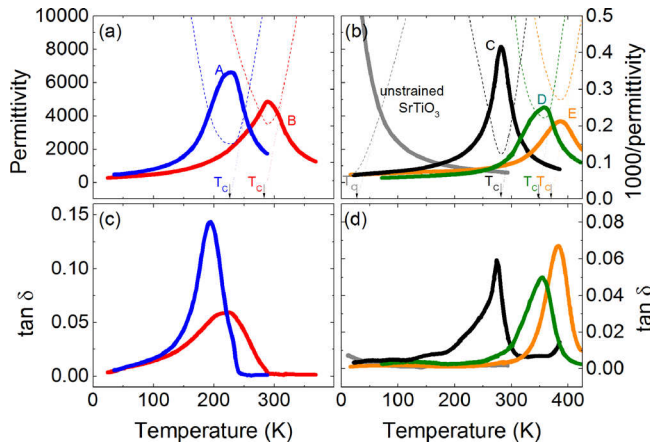


FIG. 3. Temperature dependence of the dielectric permittivity (a) and (b) and  $\tan \delta$  (c) and (d) for samples A–E (only the data for the large strain direction are displayed) and unstrained  $\text{SrTiO}_3$  (reference sample). The dashed lines in (a) and (b) show Curie-Weiss fits (plot of the inverse permittivity (right scale) vs. temperature), and the linear extrapolation provides the Curie-Weiss temperature  $T_C$ .

The resulting  $T_C$ -values are quite similar for both approaches. We get  $T_C = (33 \pm 6)$  K,  $(84 \pm 8)$  K, and  $(179 \pm 23)$  K for unstrained  $\text{SrTiO}_3$ ,  $\text{Sr}_{0.875}\text{Ba}_{0.125}\text{TiO}_3$ , and  $\text{Sr}_{0.63}\text{Ba}_{0.37}\text{TiO}_3$ , respectively. Using these values as reference values for  $T_C$  of unstrained SBTO, we obtained the resulting change of  $T_C$ .

The Landau thermodynamic theory can be used to predict the  $T_C$  enhancement due to strain.<sup>8</sup> In this approach, the shift of the transition temperature as a function of in-plane strain is given by

$$\Delta T_C = T_{C,\text{film}} - T_{C,\text{ref}} = 2\epsilon_0 C \frac{Q_{11} + Q_{12}}{s_{11} + s_{12}} \epsilon, \quad (2)$$

where  $T_{C,\text{film}}$  and  $T_{C,\text{ref}}$  are the Curie temperatures of the strained film and of the corresponding unstrained materials, respectively,  $\epsilon_0$  is the permittivity of vacuum,  $C$  is the Curie-Weiss constant,  $Q_{ij}$  and  $s_{ij}$  represent the electrostrictive coefficients and elastic compliances, and  $\epsilon$  is the strain. For the calculation, we use literature values for the parameters  $Q_{ij}$ ,  $s_{ij}$ , and  $C$  (see Table II).

Fig. 4 shows a comparison of the experimentally determined strain dependence of  $\Delta T_C$  for our SBTO films and theoretical predictions based on thermodynamic considerations using Eq. (2). The experimental results are based on the nominal strain (later, we will demonstrate that these values have to be corrected, see for instance Fig. 6). The experimental data and the theoretical prediction show the same behavior,  $\Delta T_C$  increases more or less linearly with increasing in-plane strain. The experimental data only deviate from linearity at large strain, and  $\Delta T_C$  seems to start to saturate at  $\epsilon \approx 1.2\%$ . The behavior of  $\text{BaTiO}_3$ ,  $\text{SrTiO}_3$ , and their mixture seems to

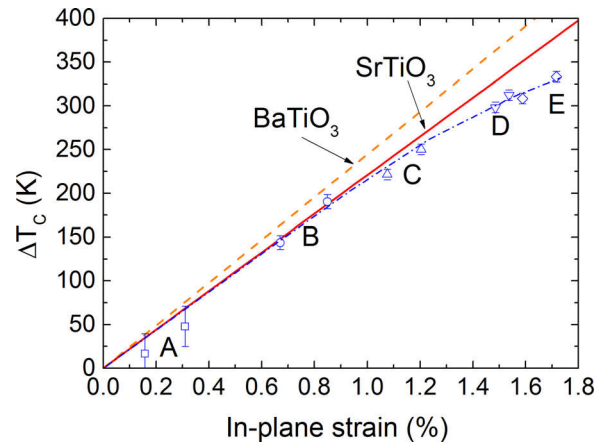


FIG. 4. Enhancement of  $T_C$  as a function of the nominal in-plane strain for samples A (squares), B (circles), C (up triangles), D (down triangles), and E (diamonds). The samples are measured along the [100] and [010] directions of the film, i.e., there are always two data points for each sample. The in-plane strain is obtained from the comparison of the measured lattice parameters and the literature value of the lattice parameter. Later, we demonstrate that this value has to be corrected (see Fig. 6 and the related discussion). The lines marked  $\text{BaTiO}_3$  and  $\text{SrTiO}_3$  represent theoretical predictions (Eq. (2)) for strained  $\text{BaTiO}_3$  and  $\text{SrTiO}_3$ , respectively. The dashed-dotted line shows the trend of the experimentally determined strain dependence of  $\Delta T_C$  for our samples (guide for the eye).

be very similar. Let us discuss the different aspects of this plot in detail. There is only a small difference between the predictions for  $\text{SrTiO}_3$  and  $\text{BaTiO}_3$ , i.e.,  $\Delta T_C$  is only slightly larger for  $\text{BaTiO}_3$ . Furthermore, both predictions already agree quite well with the experimental values. Only for large strain ( $\epsilon > 1.2\%$ ) do the measured data deviate from the theory. Compared with the theoretical prediction, it appears that the strain in the film is overestimated for  $\epsilon > 1.2\%$ . A possible reason might be that in this calculation, all kinds of strain relaxation are ignored. This will be discussed in the summary of this publication.

In order to understand the impact of strain in strained epitaxial films, possible mechanisms for strain relaxation have to be considered. One of the major contributions to strain relaxation is provided by misfit dislocations which are automatically generated during film growth due to the strain. These dislocations reduce the elastic energy, and the strain is compensated by these defects which form during film growth.<sup>34,35</sup> The equilibrium thermodynamic theories developed by van der Merwe<sup>36</sup> and Matthews and Blakeslee<sup>37</sup> predict a critical thickness  $h_c$ , below which the film grows without defects or misfit dislocations. In these theories, the total strain energy is relaxed by the termination of the misfit dislocation. The critical thickness is given by<sup>38</sup>

$$h_c = \left[ \frac{b}{4\pi(1+\nu)\epsilon_0} \right] \left[ \ln \left( \frac{h_c}{b} \right) + 1 \right], \quad (3)$$

TABLE II. Parameters used for the thermodynamic prediction of  $\Delta T_C$  (Eq. (1)) for  $\text{SrTiO}_3$  and  $\text{BaTiO}_3$ .

	$Q_{11}+Q_{12}$	$s_{11}+s_{12}$	$C$	$T_{C,\text{ref}}$
$\text{SrTiO}_3$	$-0.033 \text{ m}^4/\text{C}^2$ (Ref. 31)	$2.38 \times 10^{-12} \text{ m}^2/\text{N}$ (Ref. 32)	$9 \times 10^4 \text{ K}$ (Ref. 26)	36 K
$\text{BaTiO}_3$	$-0.065 \text{ m}^4/\text{C}^2$ (Ref. 33)	$5.65 \times 10^{-12} \text{ m}^2/\text{N}$ (Ref. 31)	$12 \times 10^4 \text{ K}$ (Ref. 26)	393 K

where  $\epsilon_0 = (a_{\text{film}} - a_{\text{substrate}})/a_{\text{film}}$  represents the lattice misfit at growth temperature (700 °C) defined by the lattice parameters of the unstrained film ( $a_{\text{film}}$ ) and the substrate ( $a_{\text{substrate}}$ ) at growth temperature,  $b$  is the extension of the dislocation line, and  $\nu$  is Poisson's ratio. We take reasonable values for  $b = 0.4$  nm, Poisson's ratio  $\nu = 0.23$  for unstrained SBTO,<sup>23</sup> or, alternatively, our experimental value  $\nu = 0.33$  for strained SBTO. Furthermore, literature values are used for the lattice parameters and thermal expansion coefficients of the film and substrates.<sup>39</sup> The resulting predictions for the critical thicknesses  $h_c$  due to dislocation formation are 11.1 nm, 9.6 nm, and 5.9 nm for SrTiO<sub>3</sub> grown on DyScO<sub>3</sub>, TbScO<sub>3</sub>, and GdScO<sub>3</sub>, respectively, along the large strain directions. Similarly, the critical thickness can be calculated for the other samples and for the small strain direction of SBTO. The resulting critical thickness is shown in Fig. 5 as a function of lattice misfit.

Generally, epitaxial films start to grow fully strained until they reach the critical thickness. Once the film reaches the critical thickness, defects develop and the strain in the next layers decreases. As a result, the total effective strain of a film is smaller than the nominal strain, once the critical thickness is exceeded. Considering this effect, the strain relaxation is larger for the films with smaller critical thickness, i.e., the films with larger lattice mismatch.

The analysis for SBTO (Fig. 5) shows that for  $\epsilon \leq 0.5\%$ , the critical thickness exceeds 40 nm, which is the thickness of our films. Therefore, we expect that sample A is fully strained with a very low density of “naturally grown” misfit dislocations. For all other samples, the critical thickness is smaller than 40 nm. As a consequence, dislocations are generated due to the larger lattice mismatch between the film and substrate in these samples. In the following, we will briefly discuss the defect-induced strain relaxation in SBTO.

The accumulation of misfit dislocations starts at the critical thickness and eventually leads to complete relaxation of the strain if the films are sufficiently thick. Based on the equilibrium thermodynamic theory, the density of misfit dislocations is given by<sup>40</sup>

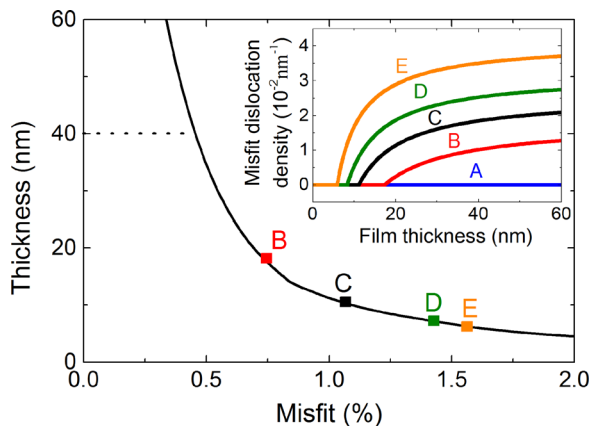


FIG. 5. Critical thickness for the generation of misfit dislocations according to Eq. (3). Only the values obtained for the large strain direction are displayed, and the critical thickness of sample A is about 157 nm, i.e., beyond the scale of the plot. The inset shows the misfit dislocation density as a function of film thickness for the large strain direction according to Eqs. (4) and (5).

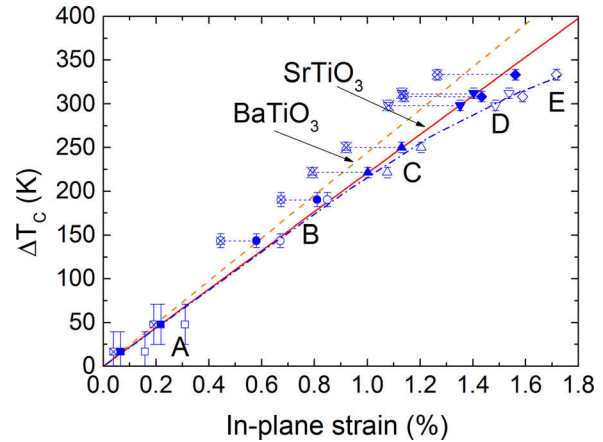


FIG. 6. Enhancement of  $T_c$  as a function of in-plane strain for samples A (squares), B (circles), C (up triangles), D (down triangles), and E (diamonds) for the large and small strain directions. The open symbols represent data based on the nominal strain (dashed-dotted line serves as a guide for the eye) shown in Fig. 4. The other symbols show the corrected values using a Poisson's ratio  $\nu = 0.23$  (solid symbols) and  $\nu = 0.33$  (open with crosses). The lines marked BaTiO<sub>3</sub> and SrTiO<sub>3</sub> represent theoretical predictions (Eq. (1)) for strained BaTiO<sub>3</sub> and SrTiO<sub>3</sub>, respectively.

$$\rho = 0, \quad \text{for } h < h_c \quad (4)$$

and

$$\rho \cong \frac{\epsilon_0}{|b| \cos \lambda} \left( 1 - \frac{h_c}{h} \right), \quad \text{for } h > h_c, \quad (5)$$

where  $|b| \cos \lambda$  is the projection of the Burgers vector of the defect to the substrate surface. By simply choosing the most common slip system [101]  $\langle 101 \rangle$  in perovskites,<sup>40</sup> we can use the lattice parameter of SrTiO<sub>3</sub> (at growth temperature) as  $|b| \cos \lambda$ .<sup>41</sup> The resulting equilibrium linear misfit dislocation density is given in the inset of Figure 5.

Obviously, misfit dislocations and other kinds of defects (e.g., oxygen vacancies<sup>42</sup>) contribute to the relaxation of the strain in the SBTO layers. The effective lattice parameter of the strained film can be approximated by<sup>23</sup>

$$a_{\text{eff}} = \frac{va + vb + (1 - \nu)c}{1 + \nu}, \quad (6)$$

where  $\nu$  is the Poisson's ratio, and  $a$ ,  $b$  are the in-plane lattice parameters and  $c$  is the out-of-plane lattice parameter. Inserting reasonable parameters, e.g.,  $\nu = 0.23$  and the experimentally determined lattice parameters (see Table II), we obtain the effective intrinsic lattice parameter. For instance, for SrTiO<sub>3</sub> grown on DyScO<sub>3</sub>, TbScO<sub>3</sub>, and GdScO<sub>3</sub> substrates, these are 3.907 Å, 3.909 Å, and 3.910 Å, respectively. Obviously, the values are slightly larger than the lattice parameter 3.904 Å for perfect (defect-free) SrTiO<sub>3</sub>.<sup>43</sup> Moreover, with increasing lattice mismatch between the film and substrate, the effective intrinsic lattice parameter also becomes larger, e.g., in our case, SrTiO<sub>3</sub> films grown on GdScO<sub>3</sub> have the largest intrinsic lattice parameter. Therefore, in order to obtain the correct strain, one has to consider the lattice parameter of the unstrained material corrected by the effective intrinsic lattice parameter.

The resulting corrected values are given in Table I and Fig. 6. Especially, Fig. 6 nicely demonstrates the improvement of the correlation between  $\Delta T_C$  and the strain obtained by the correction. The effective strain is reduced by the correction. The shift of  $T_C$  as a function of the strain becomes steeper and more linear up to the largest strain (see Fig. 6), which now is in much better agreement with the theory predicting a linear dependence of  $\Delta T_C$  on the strain.

## SUMMARY

We systematically studied the correlation between the Curie temperature and the strain in epitaxial  $\text{Sr}_{1-x}\text{Ba}_x\text{TiO}_3$  films grown on various rare-earth scandate substrates ( $\text{DyScO}_3$ ,  $\text{TbScO}_3$ , and  $\text{GdScO}_3$ ). X-ray diffraction data demonstrate that all films grow epitaxially on the different scandate substrates with a resulting in-plane tensile strain that is partially compensated by a reduction of the out-of-plane lattice parameter. The volume of the unit cell increases linearly with the in-plane areal strain. The Poisson ratio of the films turns out to be  $\nu \cong 0.33$ , i.e., larger than but still close to the literature values  $\nu = 0.23$  for unstrained defect-free  $\text{SrTiO}_3$ . The Curie temperature is extracted from temperature-dependent measurements of the dielectric response. The resulting shift of the Curie temperature agrees perfectly with the Landau thermodynamic theory if the strain relaxation due to defect formation in the films is considered.

We demonstrated that the impact of strain on the properties of ferroelectric films, especially, the Curie temperature, can be understood and predicted using relatively simple theoretical models, which consider the elastic, electrostrictive, and defect properties of the film. This approach might be useful for the tuning of the transition temperature of ferroelectric thin films and, thus, the ferroelectric properties of these materials at operating temperature, e.g., room temperature. As such, it might be a useful tool for the engineering of ferroelectric thin films in order to optimize their properties for use in various electronic applications.

## ACKNOWLEDGMENTS

The authors would like to thank A. Offenhäusser, D. Mayer, J. Schwarzkopf, S. Trelenkamp, R. Kutzner, W. Zander, T. Grellmann, K. Greben, B. Cai, and A. Markov for their valuable discussions and technical support. Financial support from the China Scholarship Council is also gratefully acknowledged.

<sup>1</sup>L. E. Cross, *Ferroelectrics* **76**, 241 (1987).

<sup>2</sup>N. Setter, D. Damjanovic, L. Eng, G. Fox, S. Gevorgian, S. Hong, A. Kingon, H. Kohlstedt, N. Y. Park, G. B. Stephenson, I. Stolitchnov, A. K. Tagantsev, D. V. Taylor, T. Yamada, and S. Streiffer, *J. Appl. Phys.* **100**, 051606 (2006).

<sup>3</sup>K. A. Müller, W. Berlinger, and E. Tosatti, *Z. Phys. B: Condens. Matter* **84**, 277 (1991).

<sup>4</sup>M. B. Smith, K. Page, T. Siegrist, P. L. Redmond, E. C. Walter, R. Seshadri, L. E. Brus, and M. L. Steigerwald, *J. Am. Chem. Soc.* **130**, 6955 (2008).

<sup>5</sup>B. Jaffe, *Piezoelectric Ceramics* (Elsevier Science, 2012).

<sup>6</sup>A. Glazer and S. Mabud, *Acta Crystallogr., Sect. B: Struct. Crystallogr. Cryst. Chem.* **34**, 1065 (1978).

<sup>7</sup>G. Shirane, R. Newnham, and R. Pepinsky, *Phys. Rev.* **96**, 581 (1954).

<sup>8</sup>J. Haeni, P. Irvin, W. Chang, R. Uecker, P. Reiche, Y. Li, S. Choudhury, W. Tian, M. Hawley, and B. Craigo, *Nature* **430**, 758 (2004).

<sup>9</sup>R. Wördenweber, E. Hollmann, R. Kutzner, and J. Schubert, *J. Appl. Phys.* **102**, 044119 (2007).

<sup>10</sup>R. Wördenweber, J. Schubert, T. Ehlig, and E. Hollmann, *J. Appl. Phys.* **113**, 164103 (2013).

<sup>11</sup>R. Wördenweber, J. Schwarzkopf, E. Hollmann, A. Duk, B. Cai, and M. Schmidbauer, *Appl. Phys. Lett.* **103**, 132908 (2013).

<sup>12</sup>B. Cai, J. Schwarzkopf, E. Hollmann, M. Schmidbauer, M. Abdel-Hamed, and R. Wördenweber, *J. Appl. Phys.* **115**, 224103 (2014).

<sup>13</sup>J. F. Ihlefeld, C. Folkman, S. Baek, G. Brennecke, M. George, J. Carroll III, and C. Eom, *Appl. Phys. Lett.* **97**, 262904 (2010).

<sup>14</sup>A. Melville, T. Mairoser, A. Schmehl, T. Birol, T. Heeg, B. Holländer, J. Schubert, C. Fennie, and D. Schlom, *Appl. Phys. Lett.* **102**, 062404 (2013).

<sup>15</sup>S. Regnery, R. Thomas, P. Ehrhart, and R. Waser, *J. Appl. Phys.* **97**, 073521 (2005).

<sup>16</sup>A. Infortuna, P. Muralt, M. Cantoni, and N. Setter, *J. Appl. Phys.* **100**, 104110 (2006).

<sup>17</sup>R. R. Das, P. Bhattacharya, and R. S. Katiyar, *Appl. Phys. Lett.* **81**, 1672 (2002).

<sup>18</sup>D. Bao, S. K. Lee, X. Zhu, M. Alexe, and D. Hesse, *Appl. Phys. Lett.* **86**, 082906 (2005).

<sup>19</sup>C. Buchal, L. Beckers, A. Eckau, J. Schubert, and W. Zander, *Mater. Sci. Eng. B* **56**, 234 (1998).

<sup>20</sup>O. Vendik, S. Zubko, and M. Nikol'skii, *Tech. Phys.* **44**, 349 (1999).

<sup>21</sup>W. Wong-Ng, Z. Yang, J. Kaduk, L. Cook, S. Diwanji, and C. Lucas, *Physica C: Superconductivity* **471**, 250 (2011).

<sup>22</sup>R. Liu, Y. Cheng, J. Chen, R. Liu, J. Wang, J. Tsai, and M. Hsu, *Mater. Lett.* **37**, 285 (1998).

<sup>23</sup>H. M. Christen, E. D. Specht, S. S. Silliman, and K. S. Harshavardhan, *Phys. Rev. B* **68**, 020101 (2003).

<sup>24</sup>L. Zhang, W. Zhong, Y. Wang, and P. Zhang, *Solid State Commun.* **104**, 263 (1997).

<sup>25</sup>S. Tinte, M. G. Stachiotti, S. R. Phillpot, M. Sepiarsky, D. Wolf, and R. L. Migoni, *J. Phys.: Condens. Matter* **16**, 3495 (2004).

<sup>26</sup>A. Hilton and B. Ricketts, *J. Phys. D: Appl. Phys.* **29**, 1321 (1996).

<sup>27</sup>S. Hoffmann and R. Waser, *J. Phys. IV France* **08**, Pr9-221–Pr9-224 (1998).

<sup>28</sup>E. Dul'kin, J. Zhai, and M. Roth, *Phys. Status Solidi B* **252**, 2079 (2015).

<sup>29</sup>G. Rupprecht and R. O. Bell, *Phys. Rev.* **125**, 1915 (1962).

<sup>30</sup>W. Jackson and W. Reddish, *Nature* **156**, 717 (1945).

<sup>31</sup>A. Kvasov and A. K. Tagantsev, *J. Appl. Phys.* **112**, 094106 (2012).

<sup>32</sup>A. Kityk, W. Schranz, P. Sondergeld, D. Havlik, E. Salje, and J. Scott, *Phys. Rev. B* **61**, 946 (2000).

<sup>33</sup>J. Wang, F. Meng, X. Ma, M. Xu, and L. Chen, *J. Appl. Phys.* **108**, 034107 (2010).

<sup>34</sup>E. Hollmann, J. Schubert, R. Kutzner, and R. Wördenweber, *J. Appl. Phys.* **105**, 114104 (2009).

<sup>35</sup>R. Wördenweber, T. Grellmann, K. Greben, J. Schubert, R. Kutzner, and E. Hollmann, *Ferroelectrics* **430**, 57 (2012).

<sup>36</sup>J. Van der Merwe, *J. Appl. Phys.* **34**, 117 (1963).

<sup>37</sup>J. Matthews and A. Blakeslee, *J. Cryst. Growth* **27**, 118–125 (1974).

<sup>38</sup>J. Matthews, D. Jackson, and A. Chambers, *Thin Solid Films* **26**, 129 (1975).

<sup>39</sup>R. Uecker, B. Velickov, D. Klimm, R. Bertram, M. Bernhagen, M. Rabe, M. Albrecht, R. Fornari, and D. G. Schlom, *J. Cryst. Growth* **310**, 2649 (2008).

<sup>40</sup>J. S. Speck and W. Pompe, *J. Appl. Phys.* **76**, 466 (1994).

<sup>41</sup>Z. G. Ban and S. P. Alpay, *J. Appl. Phys.* **91**, 9288 (2002).

<sup>42</sup>E. J. Tarsa, E. A. Hachfeld, F. T. Quinlan, J. S. Speck, and M. Eddy, *Appl. Phys. Lett.* **68**, 490 (1996).

<sup>43</sup>T. Yamanaka, N. Hirai, and Y. Komatsu, *Am. Mineral.* **87**, 1183 (2002).